Saturation of nonaxisymmetric instabilities of magnetized spherical Couette flow

E. J. Kaplan*
Helmholtz-Zentrum Dresden-Rossendorf, Dresden, Germany
(Received 21 February 2014; published 24 June 2014)

We numerically investigate the saturation of the hydromagnetic instabilities of a magnetized spherical Couette flow. Previous simulations demonstrated a region where the axisymmetric flow, calculated from a 2D simulation, was linearly unstable to nonaxisymmetric perturbations. Full, nonlinear, 3d simulations showed that the saturated state would consist only of harmonics of one azimuthal wave number, though there were bifurcations and transitions as nondimensional parameters (Re, Ha) were varied. Here, the energy transfer between different azimuthal modes is formulated as a network. This demonstrates a mechanism for the saturation of one mode and for the suppression of other unstable modes. A given mode grows by extracting energy from the axisymmetric flow, and then saturates as the energy transfer to its second harmonic equals this inflow. At the same time, this mode suppresses other unstable modes by facilitating an energy transfer to linearly stable modes.

DOI: 10.1103/PhysRevE.89.063016 PACS number(s): 47.27.er, 52.65.Kj

I. INTRODUCTION

Two spheres, one inside the other, in differential rotation with a layer of fluid between will generate a broad array of possible dynamics in the enclosed fluid, depending on the aspect ratio, the rotation rates of the spheres, and the viscosity of the fluid. If the fluid is electrically conducting and permeated by a magnetic field, applied and/or self-excited, the array of possible dynamics broadens further. The configuration, known as magnetized spherical Couette flow, was first studied numerically by Hollerbach [1] as an extension of the nonmagnetic spherical Couette problem [2,3]. Since then the flow has been investigated, numerically [4–10] and experimentally [11–14], under a variety of imposed fields and magnetic boundary conditions with sometimes surprising results. For example, in the case of a conducting inner boundary an applied magnetic field can induce a flow rotating faster than the inner sphere or rotating in the opposite direction to the inner sphere, depending on the applied field configuration [5]. The superrotating case was experimentally demonstrated in the Derviche Tourneur Sodium (DTS) experiment [10]. A compendium of magnetized spherical Couette results can be found in Ref. [15].

A long, albeit contentiously, discussed result of magnetized spherical Couette flow is the observation of an angular momentum transporting instability in a turbulent (Re $\approx 10^7$) liquid metal flow, induced by an applied axial magnetic field, that was described in Ref. [14] as the long sought after magnetorotational instability (MRI). This would be momentous as the MRI is commonly considered the mechanism by which angular momentum is removed from accretion disks around black holes, allowing matter to fall into the center. This is also potentially relevant to angular momentum transport in protoplanetary disks. The instability is driven by magnetic tension, which links together fluid parcels so that a parcel that moves outward is azimuthally accelerated, thus being pushed farther outward, and a parcel that moves inward is azimuthally decelerated, thus being pulled farther inward [17]. In contrast to the MRI as usually described [18,19], the instability measured in Ref. [14] was nonaxisymmetric and demonstrated an equatorial symmetry whose parity depended on the strength of the applied magnetic field. Subsequent numerical investigations [4,6] turned up a collection of inductionless instabilities—related to the hydrodynamic jet instability, the Kelvin-Helmholtz-like Shercliff layer instability, and a return flow instability—that replicated these parity transitions, as well as the torque on the outer sphere (the proxy measurement of angular momentum transport). Figure 1 shows the streamlines of meridional circulation and isocontours of angular momentum for the axisymmetric background flow over contours of the energy densities of the various instabilities. These instabilities were found by first evolving a two-dimensional (axisymmetric) flow to steady state at a given (Re, Ha), and then applying a linearized Navier-Stokes (LNSE) calculation to find the fastest-growing/slowest-decaying eigenmode (in a manner similar to [6]). A more modestly scaled (Re $< 10^5$), but more comprehensively diagnosed [ultrasonic Doppler velocimetry (UDV), electric potential measurements], spherical Couette experiment is being carried out at the Helmholtz-Zentrum Dresden-Rossendorf in order to better characterize these instabilities, their criteria, and their saturation. Towards that end, the Hollerbach code [20] is being run to predict the signatures of the various instabilities in the available diagnostics. Presented here is a spectral analysis of the simulations, whose intent is to explicate the saturation and transition of Shercliff and return flow instabilities through a comparatively small number of nonlinear interactions. Table I lists dimensional and nondimensional parameters of the under construction experiment, the simulations presented here, and two other spherical Couette experiments for comparison.

The flow is driven by the rotating inner sphere and evolves according to the incompressible Navier-Stokes equation:

$$\begin{aligned} \nabla \cdot \mathbf{U} &= 0, \\ \nabla \times \mathbf{U} &= \boldsymbol{\omega}, \\ \frac{\partial \boldsymbol{\omega}}{\partial t} &= \nabla \times \mathbf{F} + \nabla^2 \boldsymbol{\omega}. \end{aligned} \tag{1}$$

The body force $\mathbf{F}$ is given by

$$\mathbf{F} = \text{Re}(\nabla \times \mathbf{U}) \times \mathbf{U} + \text{Ha}^2 (\nabla \times \mathbf{B}) \times \mathbf{B}, \tag{2}$$

with $\mathbf{U}$ and $\mathbf{B}$ vector fields of the velocity and magnetic fields respectively, Re the fluid Reynolds number ($r_1^2 \Omega/\nu$, r_1 inner

*e.kaplan@hzdr.de

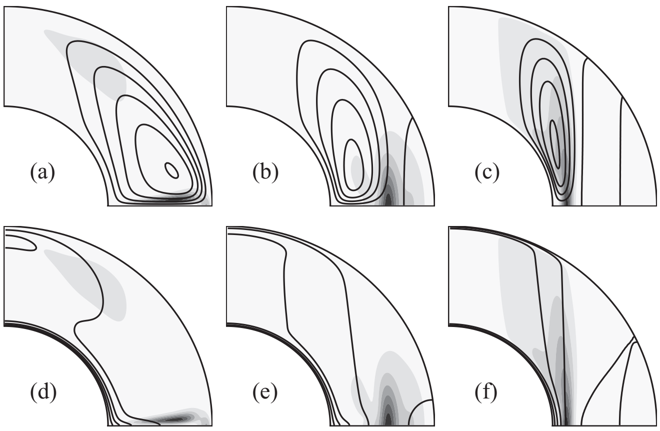

FIG. 1. Profiles of the energy density of the most unstable eigenmode from an LNSE analysis of flows at three different Hartmann numbers at Re 1100. (a)–(c) show streamlines of the meridional flow over the energy density of the $m = 2$ harmonic. (d)–(f) show contours of the angular momentum over the same. (a) and (d) show the equatorially antisymmetric jet instability (Re 1100, Ha 10). (b) and (e) show the equatorially symmetric return flow instability (Re 1100, Ha 30). (c) and (f) show the equatorially symmetric Shercliff layer instability (Re 1100, Ha 70).

radius, Ω inner sphere rotation rate, ν bulk viscosity of the fluid), and Ha the Hartmann number ($B_0 r_1 \sqrt{\sigma/\rho\nu}$, B_0 applied field strength, σ electrical conductivity, ρ mass density).

The magnetic field is split into an applied ($\mathbf{B}_0$) and an induced ($\mathbf{b}$) component, where the applied field is curl free within the flow domain. The Lorentz force is then given by

$$(\nabla \times \mathbf{B}) \times \mathbf{B} = (\nabla \times \mathbf{b}) \times \mathbf{B}_0 + (\nabla \times \mathbf{b}) \times \mathbf{b}, \qquad (3)$$

where $\mathbf{b}$ is given by the magnetic induction equation in the (so-called inductionless) limit where diffusion ($\nabla^2 \mathbf{b}$) exactly balances advection [$\nabla \times (\mathbf{U} \times \mathbf{B}_0)$]:

$$0 = \nabla^2 \mathbf{b} + \nabla \times (\mathbf{U} \times \mathbf{B}_0). \qquad (4)$$

The $(\nabla \times \mathbf{b}) \times \mathbf{b}$ term in Eq. (3) is taken to be small. The inductionless limit is valid at low magnetic Reynolds number

$$\mathrm{Rm} \equiv \frac{\tau_{\mathrm{diff}}}{\tau_{\mathrm{eddy}}} = \frac{L^2/\eta}{L/U_0} \ll 1,$$

where τ_{diff} is the magnetic diffusion time, τ_{eddy} is the large eddy turnover time, L is the characteristic scale length, η is the magnetic diffusivity, and U_0 is the characteristic velocity. This implies that magnetic fields diffuse away on such rapid time scales, relative to the flow dynamics, that they can only take the shape/value at a given instant in time that the flow would induce in that instant alone. Because the field generated in that instant must take its energy from the flow, the field generation acts as an extra drag on the development of the flow (akin, if not identical, to viscosity).

The flow is simulated using a code, described in Ref. [20], that defines the magnetic and velocity fields spectrally, in terms of vector spherical harmonics divided into toroidal and poloidal components. The magnetic boundaries are taken to be insulating (zero toroidal magnetic field outside the flow, zero jump in poloidal field at the boundaries); the flow is taken to be no-slip at the inner and outer boundaries. This paper concerns itself with only the azimuthal component of the spectral decomposition, and with interactions between different azimuthal flow modes. The simulations presented herein were run with spectral resolutions of 60 radial modes, 200 latitudinal modes, and 20 longitudinal modes, consistent with other publications [21] on the topic.

The code treats (1) pseudospectrally, with the spectra being expanded out into real space to calculate (2) and (4) and then transformed back. This is a quite normal method and usually the most efficient way to go about solving the problem (multiplications are easy in real space, derivatives are easy in spectral space). If the problem were treated spectrally, the computer time per time step would increase, but the flow would evolve identically to the pseudospectral code. The analysis presented below takes individual time steps of the pseudospectral code, and then interprets the dynamics at these time steps in terms of three-wave coupling of spectra. See Appendix A for a detailed explanation of this process.

The rest of the paper will proceed as follows. Section II provides the definition of the nonlinear interactions and an introduction to the nomenclature used to describe them. Sections III and IV below contain analyses based on networks of nonlinear interactions for the Shercliff layer instability and the return flow instability, respectively. Section V concludes the paper.

TABLE I. List of typical dimensional and nondimensional parameters for the first Maryland experiment [14], DTS [11], the (under construction) HZDR experiment, and the simulations performed here. Fluid parameters for liquid sodium and GaInSn are taken from [16].

	Maryland [14]	DTS [11]	Dresden	simulations
fluid	Na	Na	GaInSn	
ν, viscosity ($\mathrm{m^2\ s^{-1}}$)	7.4×10^{-7}	7.4×10^{-7}	2.98×10^{-7}	
ρ, density ($\mathrm{kg\ m^{-3}}$)	927	927	6360	
σ, conductivity ($\mathrm{ohm^{-1}\ m^{-1}}$)	1.0×10^{7}	1.0×10^{7}	3.1×10^{6}	
r_1, inner radius (cm)	5	7.4	3 or 4.5	
r_2, outer radius (cm)	15	21	9	
Ω, inner sphere rotation (rad $\mathrm{s^{-1}}$)	8	25	0.01	
B_0, applied magnetic field (mT)	<90 axial	62 dipole	<160 axial	axial
η, aspect ratio	0.33	0.35	0.33 or 0.5	0.33 or 0.5
Re, Reynolds number ($\Omega r_1^2/\nu$)	1.3×10^{6}	10^{5}	10^{3}	$\leqslant 1500$
Rm, magnetic Reynolds number ($\mu_0 \sigma \Omega r_1^2$)	4	10	10^{-3}	0, by construction
Ha, Hartmann number ($B_0 r_1 \sigma^{1/2} \rho^{-1/2} \nu^{-1/2}$)	5×10^{2}	5×10^{2}	$<1.6 \times 10^{2}$	<100

II. CHARACTERIZING INTERACTIONS

When considering the solution to a nonlinear differential equation one typically looks for some characterizing value from which a meaningful interpretation of the evolution can be made. Previous magnetized spherical-Couette studies [4,5] drew their conclusions from the torque on the outer sphere, in part because a physical experiment would have access to that measurement directly. Other studies [6,21] used the energies contained in individual azimuthal modes to demonstrate transitions between different states as the nondimensional parameters were varied. Here, we are going to propose the three-wave coupling between azimuthal modes, complex as it may be to fully consider, as the relevant characterization. A similar characterization was done in Ref. [22] for a kinematic dynamo problem. There the velocity field catalyzed the interactions of magnetic modes, but was itself unaffected (as per the definition of kinematic dynamo problem); here the velocity modes are the catalysts *and* the reactants.

We start by defining an inner product, which mode energies and energy transfers will be defined with, by the volume integral of two vector fields dotted together:

$$\langle \mathbf{A},\mathbf{B}\rangle = \int_1^{1/\eta} dr\, r^2 \int_0^{\pi} d\theta\, \sin\theta \int_0^{2\pi} d\phi\, \mathbf{A}(r,\theta,\phi)\cdot\mathbf{B}(r,\theta,\phi). \tag{5}$$

From this we define the energy contained in each mode

$$E^m = \tfrac{1}{2}\langle \mathbf{U}^m,\mathbf{U}^m\rangle, \tag{6}$$

with the change in energy in a given mode from some small change given by the Taylor expansion:

$$\delta E^m = \langle \mathbf{U}^m,\boldsymbol{\delta}^m\rangle, \tag{7}$$

where $\boldsymbol{\delta}^m$ is a small perturbation to the velocity field of azimuthal mode m.

The individual $\boldsymbol{\delta}^m$s to be considered come from the forcing Eq. (2), which can be broken up into a collection of interactions between individual m modes represented by the effect of the coupling on the target mode:

$$(a,b\to c) = \langle[(\nabla\times\mathbf{U}^a)\times\mathbf{U}^b + (\nabla\times\mathbf{U}^b)\times\mathbf{U}^a],\mathbf{U}^c\rangle; \tag{8}$$

i.e., the addition or reduction of energy in mode c from the beating of modes a and b defines $(a,b\to c)$. The energy dynamics can also be considered in terms of a transfer from one mode to another, mediated by a third. This is represented by $(a \xrightarrow{b} c)$, which represents energy being removed from mode a and deposited in mode c through the interaction with mode b. To use the language of graph theory, $\xrightarrow{b}$ is an edge connecting two nodes a and c. Typically $(c \xrightarrow{a} b)$ and $(b \xrightarrow{c} a)$ are also nonzero. Throughout this paper, interaction will be used as a general term for both beats and edges.

This analysis assumes that the change in energy in a given mode during a given time step is well represented by the linear sum of individual nonlinear interactions between modes

$$\gamma c \equiv \frac{\partial E^c}{\partial t} \approx \frac{E^c(t+\delta t)-E^c(t)}{\delta t} \approx \sum_{a,b}\frac{(a,b\to c)}{\delta t}; \tag{9}$$

that the interactions between a given triplet of modes (a, b, and c) only act to redistribute energy among them,

$$(a,b\to c)+(b,c\to a)+(c,a\to b)=0; \tag{10}$$

and that energy is only added to or removed from the instability through interaction with the axisymmetric background,

$$\frac{\partial \sum_m E^m}{\partial t} = \sum_m (m,0\to m), \tag{11}$$

where all other interactions only act to redistribute energy between the various modes. All three assumptions are checked numerically as the analysis code is run and have heretofore held to within one percent.

The consequence of (10) is that any given triplet of beats can be represented entirely by two edges. For a triplet with $a\neq b\neq c$, one beat of $(a,b\to c)$, $(b,c\to a)$, and $(c,a\to b)$ will have a larger magnitude than and opposite sign to the others. For $(a,b\to c)>0$, mode c is acting as an energy sink, and drawing energy (unevenly) from modes a and b. This can be represented by two edges

$$(a \xrightarrow{b} c) = -(b,c\to a),$$
$$(b \xrightarrow{a} c) = -(c,a\to b),$$

where $(m_1 \xrightarrow{m_2} m_3)$ is the energy drawn from m_1 and deposited in m_3 from the triplet. For $(a,b\to c)<0$, mode c is acting as an energy sink and depositing energy (unevenly) into modes a and b, which is represented as

$$(c \xrightarrow{b} a) = (b,c\to a),$$
$$(c \xrightarrow{a} b) = (c,a\to b).$$

The transfer from m_1 to m_2 or vice versa is accounted for by the difference between $(m_1 \xrightarrow{m_2} m_3)$ and $(m_2 \xrightarrow{m_1} m_3)$.

When describing the edges, all diffusive effects are included with the axisymmetric flow, i.e., as a part of $(a \xrightarrow{0} a)$. While viscous diffusion as accounted for in the code communicates energy between radial modes/nodes, it does not communicate between different latitudinal or azimuthal modes. In the discussion to follow, magnetic effects will also be included as a part of $(a \xrightarrow{0} a)$. Because $\mathbf{B}_0$ is axisymmetric in all simulations presented, both $\nabla\times(\mathbf{U}^a\times\boldsymbol{B}_0)$ and $(\nabla\times\mathbf{b}^a)\times\mathbf{B}_0$ have zero projection onto any mode $m\neq a$. Similarly, if quadratic effects of the induced magnetic field [the $(\nabla\times\mathbf{b})\times\mathbf{b}$ term in Eq. (3)] were included, they would be folded into the $(a \xrightarrow{a} 2a)$ and $(a \xrightarrow{a} 0)$ edges.

The purpose of these assumptions is to allow the nonlinear dynamics of the flow to be represented in terms of a network of interactions. This network formulation is applicable for any system where there is some global quantity, such as energy or helicity, for which the presence in a given mode of a dynamic system is quantifiable, and for which the transfer of this quantity between modes is also quantifiable. Once a list of edges and nodes has been generated, there are open source tools to visualize the graph. Here we make use of GRAPHVIZ [23].

Sections III and IV below contain analyses based on such networks. In these analyses there is sometimes reference made to λm. This represents a guess of the growth rate of mode m based on

$$\lambda m = e_m E^m, \tag{12}$$

where e_m is the eigenvalue of the fastest-growing/slowest-decaying eigenmode of the LNSE analysis. The guess assumes that the flow found for the given m in the fully 3d calculation is identical to that eigenmode. This is a good assumption only if $(m \xrightarrow{0} m) = \lambda m = \gamma m$.

As the Shercliff layer instability has the simplest network, that is where we shall begin.

III. SATURATION OF THE SHERCLIFF LAYER INSTABILITY

The Shercliff layer is a shear layer that arises in spherical Couette flows where the magnetic field is strong enough to force the fluid inside the inner sphere's tangent cylinder to corotate with the inner sphere. The fluid outside the tangent cylinder is in corotation with the outer sphere (i.e., at rest in our simulations). The instability that can arise in this context [see Figs. 1(c) and 1(f)] is akin to a Kelvin-Helmholtz instability, and was studied fairly extensively in Ref. [5].

Figure 2 shows the energy content of each azimuthal mode for a run with $\eta = 0.5$, Re = 1000, Ha = 70. This is where the $m = 2$ mode is unstable, but the $m = 3$ mode is (just barely) still stable. The bulk of the energy lives in the $m = 2$ azimuthal mode, which grows exponentially and then begins to asymptote around $t = 80$. The higher harmonics of $m = 2$ grow alongside the first harmonic, and begin to saturate at the same time. The energies in the odd modes are all much much smaller than those in the even modes, and as the even modes asymptote, the odd modes begin to decay roughly exponentially.

Figure 3 shows the network of interactions at a point during the saturation phase of the instability. This is made up only of the harmonics of $m = 2$. Herein lie examples

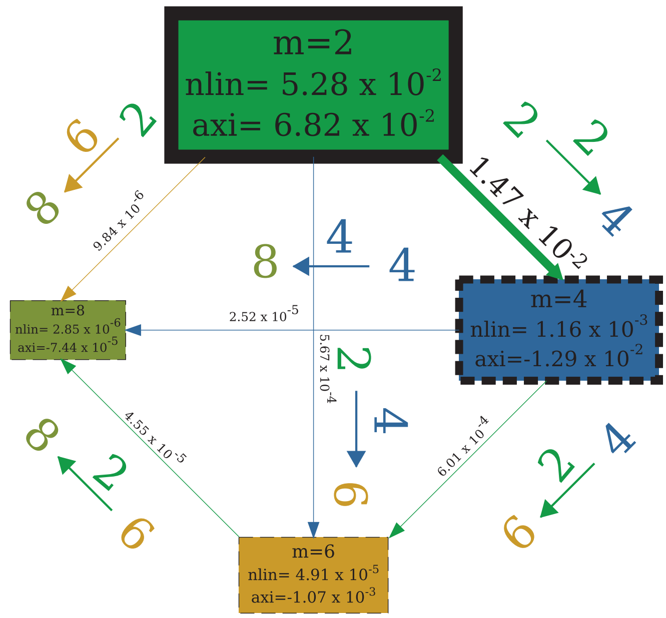

FIG. 3. (Color) Network of interactions for the time indicated in Figs. 2, 4, and 5. The diagram should be interpreted as follows. The color of each arrow indicates b in $(a \xrightarrow{b} c)$. Here the interactions are also written out explicitly along the edges. The size of each box scales with the logarithm of the energy in the mode at the given time step. The numbers indicated by nlin and axi are, respectively, the $\frac{\partial E^m}{\partial t}$ of the mode for the full simulation and the influence of the axisymmetric component $(m \xrightarrow{0} m)$. The strength of the connection $a \xrightarrow{b} c$ is written along the edge. The width of each edge scales with the logarithm of the connection strength. The black border of each node is scaled with the logarithm of the magnitude of $(m \xrightarrow{0} m)$, with dashed lines indicating an energy sink and a solid line indicating an energy source. The nodes are limited to $a,c \in \{2,4,6,8\}$; the edges are limited to $b \in \{2,4,6\}$.

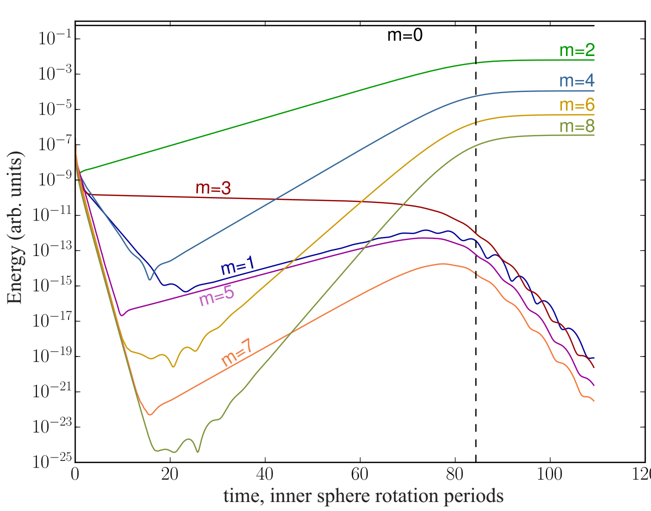

FIG. 2. (Color online) Time series of energies contained in each azimuthal mode for a simulation with $\eta = 0.5$, Re = 1000, Ha = 70. The vertical line indicates the time slice the network diagram in Fig. 3 is made from.

of most of the types of edges that will be of interest. For example, $(2 \xrightarrow{2} 4)$ and $(4 \xrightarrow{4} 8)$ represent modes interacting with themselves nonlinearly and depositing energy into their second harmonic. Modes $m = 6$ and $m = 8$ are both acting as sinks $[(2 \xrightarrow{4} 6 \xleftarrow{2} 4),(2 \xrightarrow{6} 8 \xleftarrow{2} 6)]$. The vast majority of the dynamics are contained in the $(2 \xrightarrow{0} 2),(2 \xrightarrow{2} 4)$, and $(4 \xrightarrow{0} 4)$ edges. This dominance is demonstrated more clearly in Fig. 4, where the growth of $m = 2$ is indistinguishable from $(2 \xrightarrow{0} 2)$ until $t \approx 80$. At this point $(2 \xrightarrow{2} 4)$ is on the same order of magnitude as $(2 \xrightarrow{0} 2)$, and from there on out the two edges asymptote towards each other. The energy being deposited in $m = 4$ is almost completely dissipated by the background flow. The next largest edge $[(4 \xrightarrow{2} 6)$, not shown] has an impact an order of magnitude weaker than $(4 \xrightarrow{0} 4)$.

The odd modes are even simpler. Figure 5 shows a time series of the edges relevant for $m = 3$, and there are few. Until $t \approx 60$ the decay rate is indistinguishable from $(3 \xrightarrow{0} 3)$, at which point $(1 \xleftarrow{2} 3 \xrightarrow{2} 5)$ is large enough to notice on the log scale. However, once the $m = 2$ harmonics start saturating the

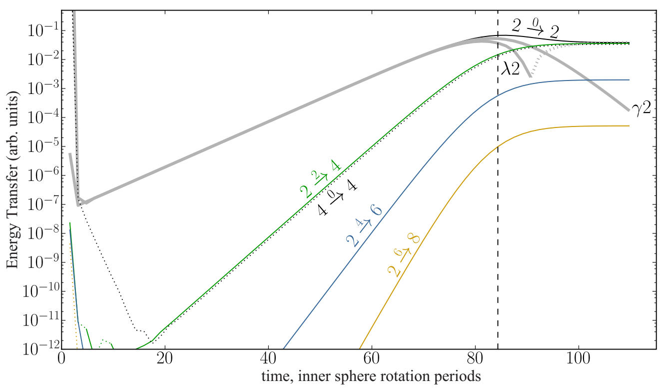

FIG. 4. (Color online) Time series of a subset of the edges from the simulation of Fig. 2 on a semilog plot. The dotted lines indicate a negative value. The bold lines labeled $\gamma 2$ and $\lambda 2$ represent the growth rates defined by Eqs. (9) and (12), respectively. The interaction $(4 \stackrel{0}{\rightarrow} 4)$ represents a decay slightly faster than that predicted by $\lambda 4$ (not pictured). The vertical dashed line indicates the time step Fig. 3 was made from.

m_{odd} modes crash, and the decay rate returns to being a near match of $(3 \stackrel{0}{\rightarrow} 3)$.

IV. SATURATION OF THE RETURN FLOW INSTABILITY

At lower Ha, the equatorial jet is no longer suppressed, but neither does it reach the edge of the sphere. Instead it returns somewhere in between r_1 and r_2 with a stagnation point on the equator. The return flow instability arises in this stagnation region [see Figs. 1(b) and 1(e)].

The two dynamics that the network characterization seeks to describe are the saturation of the dominant mode, and the suppression of the subdominant modes that are still linearly unstable. In both cases it can be shown that the network of interactions transfers energy from the unstable modes (wherein it is created) to stable modes (wherein it is destroyed). Figure 6 shows the evolution of the flow from an initial state (found by evolving an axisymmetric flow with Re = 1000, Ha = 30,

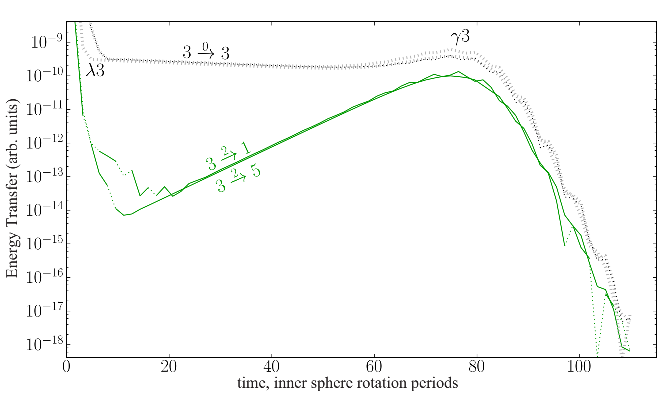

FIG. 5. (Color online) Time series of a subset of the edges from the simulation of Fig. 2 on a semilog plot. The dotted lines indicate a negative value. The bold lines labeled $\gamma 3$ and $\lambda 3$ represent the growth rates defined by Eqs. (9) and (12), respectively. The vertical dashed line indicates the time step Fig. 3 was made from.

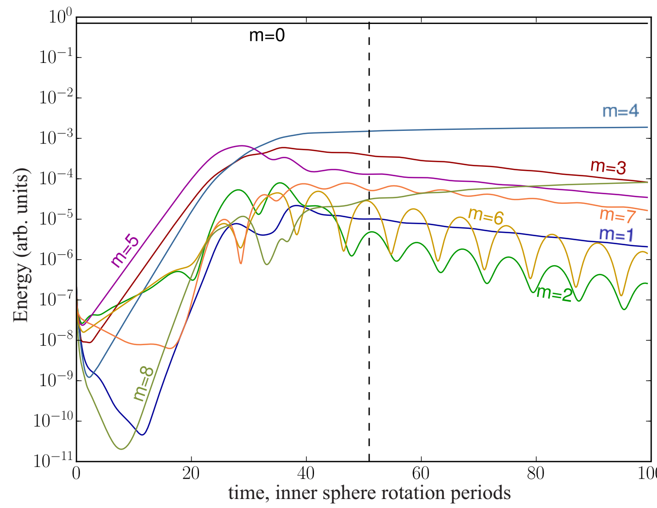

FIG. 6. (Color online) Time series of energies contained in each azimuthal mode for a simulation with $\eta = 0.5$, Re = 1000, Ha = 30. The vertical line indicates the time slice the network diagram in Fig. 7 is made from.

$\eta = 0.5$ to steady state), seeded with random nonaxisymmetric noise, to what is taken to be saturation. Up until $t \approx 15$, $m \in [2,6]$ seem to all be growing exponentially. Until about $t \approx 25$, $m \in [3,5]$ continue to grow roughly exponentially. From $t \approx 25$ on several changes can be observed. First $m = 5$ rolls over and begins to decay, then $m = 3$ rolls over and begins to decay as $m = 4$ begins to saturate.

This is where the network formulation comes into play. Figure 7 shows the network of interactions at a single point in time. Several dynamics are visible here. The $m = 4$ mode is sourcing energy and depositing much of it in its second harmonic via $(4 \stackrel{4}{\rightarrow} 8)$. The $m = 3$ mode sources energy as well, but it is a net loser of energy as more is being sent to energy dissipating modes via $(7 \stackrel{4}{\leftarrow} 3 \stackrel{4}{\rightarrow} 1)$. The $m = 1$ mode dissipates energy but is likely more significant as a path for energy to move between $m = 3$,4, and 5.

From the diagram we choose interesting edges to track over time. Figure 8 shows the dominant edges which transfer energy to or from the $m = 4$ mode, with the addition of the total growth rate, and the $(8 \stackrel{0}{\rightarrow} 8)$ and $(1 \stackrel{0}{\rightarrow} 1)$ edges. Up until $t \approx 25$, there is exponential growth which is almost entirely identical to the $(4 \stackrel{0}{\rightarrow} 4)$ term. Until $t \approx 40$, the growth is still almost entirely identical to the $(4 \stackrel{0}{\rightarrow} 4)$ term, but this edge has begun to roll over and asymptote. There are 4 edges between $t \approx 40$ and the end of the simulation that account for the vast majority of the dynamics of the $m = 4$ mode: $(4 \stackrel{3}{\rightarrow} 1)$ initially draws the largest part of the energy from $m = 4$; $(4 \stackrel{4}{\rightarrow} 8)$ dominates at long times; $(4 \stackrel{5}{\rightarrow} 9)$ and $(1 \stackrel{5}{\rightarrow} 4)$ are roughly equal, indicating that they are better considered as a single action $(1 \stackrel{5}{\rightarrow} 4 \stackrel{5}{\rightarrow} 9)$ which does not matter much in the energy dynamics of $m = 4$ itself. All but a small, and diminishing, component of the energy transferred to $m = 8$ is removed by $(8 \stackrel{0}{\rightarrow} 8)$. There is, on the other hand, a rather stable relationship between

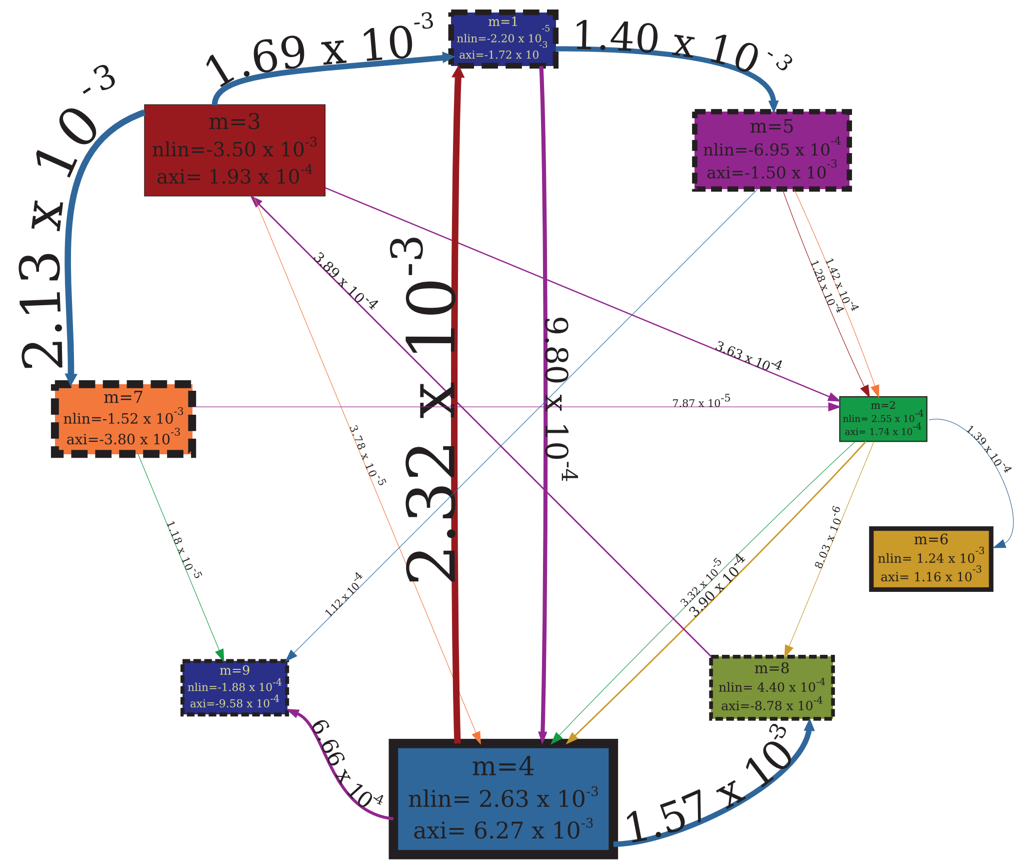

FIG. 7. (Color) Full network of interactions from the time step indicated in Fig. 6. The diagram should be interpreted as in Fig. 3. The nodes are limited to $a,c \in [1,9]$; the edges are limited to $b \in [2,7]$. A tabular form of the information is in Appendix B; Table II contains the information contained in the nodes; Table III contains a list of edge strengths.

the amount of energy transferred into $m = 1$ by $(4 \xrightarrow{3} 1)$, the amount removed by $(1 \xrightarrow{0} 1)$, and the total growth rate $\frac{\partial E^{m=4}}{\partial t}$.

The rest of the story is contained in Fig. 9. Like $m = 4$, $m = 3$ grows exponentially until $t \approx 25$ from $(3 \xrightarrow{0} 3)$. However, a gap opens up between the total growth rate and the energy drawn from the axisymmetric flow here, and from $t \approx 40$ onward there is a net loss of energy from the $m = 3$ mode, despite the fact that the mean flow is a constant source of energy.

The majority of the energy flow out of $m = 3$ is described by $(3 \xrightarrow{4} 7)$ and $(3 \xrightarrow{4} 1)$. The $m = 7$ mode is very stable, and loses more energy to the background flow than is deposited by $(3 \xrightarrow{4} 7)$. The $m = 1$ mode is also stable, but its energy

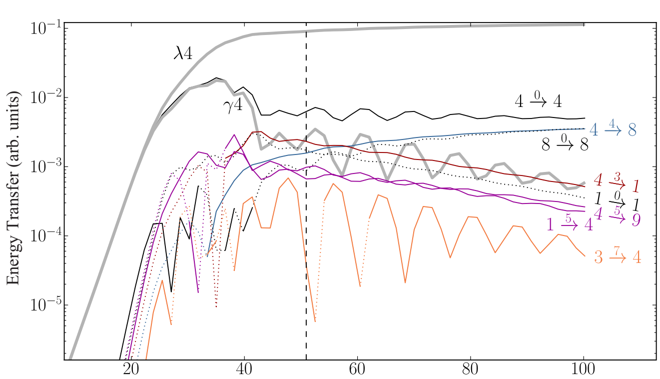

FIG. 8. (Color online) Time series of a subset of the edges from the simulation of Fig. 6 on a semilog plot. The dotted lines indicate a negative value. The bold lines labeled $\gamma 4$ and $\lambda 4$ represent the growth rates defined by Eqs. (9) and (12), respectively. The vertical line indicates the time slice the network diagram in Fig. 7 is made from.

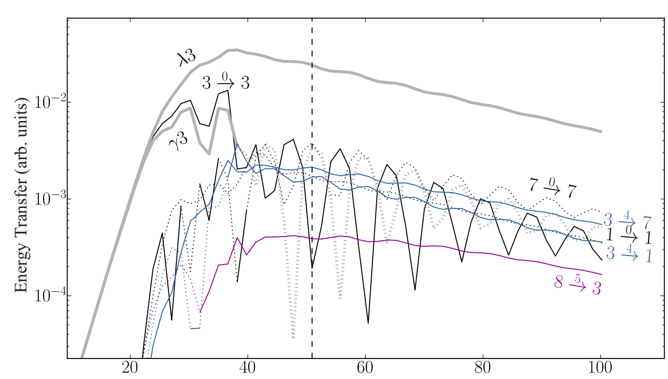

FIG. 9. (Color online) Time series of a subset of the three-wave couplings from the simulation of Fig. 6 on a semilog plot. The dotted lines indicate a negative value. The bold lines labeled $\gamma 3$ and $\lambda 3$ represent the growth rates defined by Eqs. (9) and (12), respectively. The vertical line indicates the time slice the network diagram in Fig. 7 is made from.

dissipation tends to match the energy deposited by $(3 \xrightarrow{4} 1)$ almost exactly.

V. CONCLUSIONS

The saturation of the Shercliff layer (η 0.5, Re 1000, Ha 70) and return flow (η 0.5, Re 1000, Ha 30) instabilities are characterized by the three-wave coupling between azimuthal modes (m). In both cases energy is generated by $(m \xrightarrow{0} m)$, dissipated by $(2m \xrightarrow{0} 2m)$, and transferred between the two by $(m \xrightarrow{m} 2m)$. Furthermore, in the case of the return flow instability, the dominant mode suppresses other unstable modes by facilitating a transfer of energy into higher order modes which then dissipate the energy. This suppression is a possible candidate for the hysteresis cycles of [6].

The network diagram is instrumental in this form of analysis. For a simulation with 20 azimuthal modes, there are 400 possible interactions satisfying $c = |a \pm b|$. The diagram provides a snapshot of interactions meeting certain criteria (nodes or edges as members of a chosen set, displayed edges accounting for 90% of the total energy flow). Interactions can be picked from this snapshot and tracked throughout the simulation to see how they evolve and how they relate to the final saturated state.

This formulation can be extended, at a price. Here we defined the nodes only by azimuthal order m; in Ref. [22] the nodes were further divided into degree (l), phase (sine and cosine), and toroidal/poloidal character. This was sensible there because the number of distinct edges was limited to the (four) harmonics of the defined flow, and because individual edges or series of edges could be connected to the α and Ω effects of dynamo theory. The case of magnetized inductionless spherical Couette flow would most likely not benefit from the full decomposition. However, it may still be meaningful to distinguish between equatorially symmetric ($l \in [m, m+2, \ldots, l_{\max}]$) and antisymmetric ($l \in [m+1, m+3, \ldots, l_{\max}-1]$) modes, as these classes of flow modes are excited or suppressed in different regions of the (Re, Ha) phase space.

The work presented here and that presented in Ref. [22] only cover the cases where energy transfer is facilitated by velocity modes (here between the velocity modes themselves, in Ref. [22] between magnetic modes). This network formulation is applicable for any system where there is some global quantity, such as energy or helicity, for which the presence in a given mode of a dynamic system is quantifiable, and for which the transfer of this quantity between modes is also quantifiable. As a further example, one could consider a saturating dynamo. A typical simulation, such as those in Ref. [24], will show anticorrelations between the energies in the velocity and magnetic fields, which implies that there is energy being transferred between them. The primary decisions are how the modes are defined and how the edges are calculated.

ACKNOWLEDGMENTS

The author would like to thank Rainer Hollerbach for providing the source code from [20]; Rainer Hollerbach and Andre Giesecke are also thanked for acting as "round 0" reviewers for the manuscript. This work was supported as part of the DRESDYN project [25] under Frank Stefani at the Helmholtz-Zentrum Dresden-Rossendorf. This work is supported by the Deutsche Forschungsgemeinschaft under Grant No. STE 991/1-2.

APPENDIX A: TAYLOR EXPANSION OF NONLINEAR INTERACTIONS

Hollerbach [20] describes the time evolution of the velocity field in terms of a modified second-order Runga-Kutta method, with

$$\mathbf{X}\tilde{\mathbf{v}}(t+\delta t) = \mathbf{Y}\mathbf{v}(t) + \delta t\mathbf{DV}, \tag{A1}$$

$$\mathbf{X}\mathbf{v}(t+\delta t) = \mathbf{Y}\mathbf{v}(t) + \frac{\delta t}{2}\left(\mathbf{DV}' + \mathbf{DV}\right), \tag{A2}$$

with $\mathbf{v}$ comprising both the toroidal and poloidal modes ($\mathbf{e}$ and $\mathbf{f}$ in Ref. [20]), $\mathbf{X}$ and $\mathbf{Y}$ operators that only connect k terms in the spectra with the same l and m, and $\mathbf{DV}$ and $\mathbf{DV}'$ representing the forcing on a given k,l,m spectrum. For the purposes of the Taylor expansion we are only going to deal with the predictor term. The forcing is given by

$$\mathbf{F}^{a,b}(r,\theta,\phi) = \mathrm{Re}[\nabla \times \mathbf{U}^a(r,\theta,\phi)] \times \mathbf{U}^b(r,\theta,\phi) + \mathrm{Re}[\nabla \times \mathbf{U}^b(r,\theta,\phi)] \times \mathbf{U}^a(r,\theta,\phi). \tag{A3}$$

There are three transformations to get from the spectral representation the flow is stored in to the spatial representation the force is calculated in:

$$\mathbf{U}_l^m(r) = \sum_k T_{k,l}(r)\mathbf{v}_{k,l}^m, \tag{A4}$$

$$\mathbf{U}^m(r,\theta) = \sum_l P_l^m(\theta)\mathbf{U}_l^m(r), \tag{A5}$$

$$\mathbf{U}(r,\theta,\phi) = \mathcal{F}^{-1}\{\mathbf{U}^m(r,\theta)\}, \tag{A6}$$

where $\mathcal{F}^{-1}$ is an inverse Fourier transform, P_l^m is an expansion in associated Legendre polynomials, and $T_{k,l}$ is an expansion in Chebyshev polynomial that may be slightly modified to calculate the curl of the spectrum. After the forcing is calculated in real space it is reverted to the spectral representation through another 3 transformations:

$$\mathbf{F}^m(r,\theta) = \mathcal{F}\{\mathbf{F}(r,\theta,\phi)\}, \tag{A7}$$

$$\mathbf{F}_l^m(r) = \sum_l \mathcal{P}_l^m(\theta)\mathbf{F}^m(r,\theta), \tag{A8}$$

$$\mathbf{DV}_{k,l}^m = \sum_k \mathcal{T}_{k,l}(r)\mathbf{F}_l^m(r), \tag{A9}$$

where $\mathcal{F}$ is a Fourier transform, and $\mathcal{P}_l^m$ and $\mathcal{T}_{k,l}$ transform the spatial function into Chebyshev and Legendre spectra with some curls of $\mathbf{F}$ included. The only place where there is communication between m modes is between (A6) and (A7), which allows us to treat the predictor step [Eq. (A1)] as

$$\mathbf{X}\tilde{v}^m(t+\delta t) = \mathbf{Y}v^m(t) + \delta t\sum_{a,b}\mathbf{DV}^{a,b,m}, \tag{A10}$$

where $\mathbf{DV}^{a,b,m}$ is the forcing from (A3), projected onto m. The three-wave coupling defined in Eq. (8) is given by

$$(a,b \to m) = \delta t\mathbf{X}^{-1}\mathbf{DV}^{a,b,m},$$

which is nonzero only for $m = |a \pm b|$.

TABLE II. Tabular form of network diagram of Fig. 7. List of nodes and their associated energies, nonlinear growth rates, and the action of the axisymmetric flow. The entries are sorted by azimuthal mode number.

mode	energy	nonlinear	axisymmetric
1	1.01×10^{-5}	-2.20×10^{-5}	-1.72×10^{-3}
2	2.70×10^{-6}	2.55×10^{-4}	1.74×10^{-4}
3	4.09×10^{-4}	-3.50×10^{-3}	1.93×10^{-4}
4	1.47×10^{-3}	2.63×10^{-3}	6.27×10^{-3}
5	1.31×10^{-4}	-6.95×10^{-4}	-1.50×10^{-3}
6	2.42×10^{-5}	1.24×10^{-3}	1.16×10^{-3}
7	6.34×10^{-5}	-1.52×10^{-3}	-3.80×10^{-3}
8	2.70×10^{-5}	4.40×10^{-4}	-8.78×10^{-4}
9	1.02×10^{-5}	-1.88×10^{-4}	-9.58×10^{-4}

APPENDIX B: NETWORK OF INTERACTIONS IN TABLE FORM

The networks of Figs. 3 and 7 are difficult to read. They are, however, a good graphical snapshot of where energy is moving in a nonlinear process where there is no obvious hierarchy of interactions. Table II could be sorted by mode index, as it is, or by any of the entries in the table and still be easily interpreted; there is no hierarchy of keys in Table III that reveals multistep interactions ($a \xrightarrow{b} c \xrightarrow{d} e$) as completely as Fig. 7.

TABLE III. Tabular form of network diagram of Fig. 7. List of edges and their strengths. The entries are sorted by source, edge, and target.

edge	strength	edge	strength	edge	strength
$1 \xrightarrow{4} 5$	1.40×10^{-3}	$3 \xrightarrow{4} 1$	1.69×10^{-3}	$6 \xrightarrow{3} 3$	1.15×10^{-4}
$1 \xrightarrow{5} 4$	9.80×10^{-4}	$3 \xrightarrow{4} 7$	2.13×10^{-3}	$6 \xrightarrow{7} 1$	5.23×10^{-5}
$1 \xrightarrow{5} 6$	1.70×10^{-4}	$3 \xrightarrow{5} 2$	3.63×10^{-4}	$7 \xrightarrow{2} 9$	1.18×10^{-5}
$1 \xrightarrow{6} 5$	1.24×10^{-4}	$3 \xrightarrow{7} 4$	3.78×10^{-5}	$7 \xrightarrow{5} 2$	7.87×10^{-5}
$2 \xrightarrow{2} 4$	3.32×10^{-5}	$4 \xrightarrow{3} 1$	2.32×10^{-3}	$7 \xrightarrow{6} 1$	1.12×10^{-4}
$2 \xrightarrow{3} 1$	3.20×10^{-5}	$4 \xrightarrow{4} 8$	1.57×10^{-3}	$8 \xrightarrow{5} 3$	3.89×10^{-4}
$2 \xrightarrow{4} 6$	1.39×10^{-4}	$4 \xrightarrow{5} 9$	6.66×10^{-4}	$8 \xrightarrow{7} 1$	6.59×10^{-5}
$2 \xrightarrow{6} 4$	3.90×10^{-4}	$5 \xrightarrow{3} 2$	1.28×10^{-4}	$9 \xrightarrow{6} 3$	4.31×10^{-5}
$2 \xrightarrow{6} 8$	8.03×10^{-6}	$5 \xrightarrow{4} 9$	1.12×10^{-4}		
$3 \xrightarrow{2} 1$	7.79×10^{-5}	$5 \xrightarrow{7} 2$	1.42×10^{-4}		

[1] R. Hollerbach, Proc. R. Soc. London, Ser. A **444**, 333 (1994).
[2] K. Stewartson, J. Fluid Mech. **26**, 131 (1966).
[3] I. Proudman, J. Fluid Mech. **1**, 505 (2006).
[4] C. Gissinger, H. Ji, and J. Goodman, Phys. Rev. E **84**, 026308 (2011).
[5] R. Hollerbach and S. Skinner, Proc. R. Soc. London, Ser. A **457**, 785 (2001).
[6] R. Hollerbach, Proc. R. Soc. London, Ser. A **465**, 2003 (2009).
[7] X. Wei and R. Hollerbach, Phys. Rev. E **78**, 026309 (2008).
[8] W. Liu, Phys. Rev. E **77**, 056314 (2008).
[9] E. Dormy, D. Jault, and A. M. Soward, J. Fluid Mech. **452**, 263 (2002).
[10] E. Dormy, P. Cardin, and D. Jault, Earth Planet. Sci. Lett. **160**, 15 (1998).
[11] D. Brito, T. Alboussière, P. Cardin, N. Gagnière, D. Jault, P. La Rizza, J.-P. Masson, H.-C. Nataf, and D. Schmitt, Phys. Rev. E **83**, 066310 (2011).
[12] D. H. Kelley, S. A. Triana, D. S. Zimmerman, and D. P. Lathrop, Phys. Rev. E **81**, 026311 (2010).
[13] H.-C. Nataf, T. Alboussière, D. Brito, P. Cardin, N. Gagnière, D. Jault, and D. Schmitt, Phys. Earth Planet. Inter. **170**, 60 (2008).
[14] D. R. Sisan, N. Mujica, W. A. Tillotson, Y.-M. Huang, W. Dorland, A. B. Hassam, T. M. Antonsen, and D. P. Lathrop, Phys. Rev. Lett. **93**, 114502 (2004).
[15] G. Rüdiger, L. L. Kitchatinov, and R. Hollerbach, *Magnetic Processes in Astrophysics: Theory, Simulations, Experiments* (Wiley-VCH, Weinheim, 2013), pp. 287–326.
[16] N. B. Morley, J. Burris, L. C. Cadwallader, and M. D. Nornberg, Rev. Sci. Instrum. **79**, 056107 (2008).
[17] H. Ji and S. Balbus, Phys. Today **66**(8), 27 (2013).
[18] S. A. Balbus and J. F. Hawley, Rev. Mod. Phys. **70**, 1 (1998).
[19] S. A. Balbus and J. F. Hawley, Astrophys. J. **376**, 214 (1991).
[20] R. Hollerbach, Int. J. Numer. Methods Fluids **32**, 773 (2000).
[21] V. Travnikov, K. Eckert, and S. Odenbach, Acta Mech. **219**, 255 (2011).
[22] E. J. Kaplan, B. P. Brown, K. Rahbarnia, and C. B. Forest, Phys. Rev. E **85**, 066315 (2012).
[23] E. R. Gansner and S. C. North, Journal of Software: Practice and Experience **30**, 1203 (2000).
[24] K. Reuter, F. Jenko, and C. Forest, New J. Phys. **11**, 013027 (2009).
[25] F. Stefani, S. Eckert, G. Gerbeth, A. Giesecke, T. Gundrum, C. Steglich, T. Weier, and B. Wustmann, Magnetohydrodynamics **48**, 103 (2012).